



Effects of laser fluence on near-field surface nanostructuring

Xuhui Feng^a, Xinwei Wang^{b,*}

^a *Department of Mechanical Engineering, The University of Nebraska-Lincoln,
N104 Walter Scott Engineering Center, Lincoln, NE 68588-0656, USA*

^b *Department of Mechanical Engineering, Iowa State University, 3027 H.M.
Black Engineering Building, Ames, IA 50011-2161, USA*

Received 23 September 2007; accepted 1 January 2008

Available online 12 January 2008

Abstract

In this work, molecular dynamics simulation is performed to explore the long-time (up to 5 ns) behavior of argon crystal in surface nanostructuring with an extremely localized near-field laser beam. The surface nanostructuring region is limited to tens of nanometers in diameter, although the simulated systems are much larger (comprised of more than 770,000 atoms). This study focuses on the long-time solidification and crystallization procedure, which is driven by the heat conduction in the material. The effect of the computational domain on the final nanostructure is studied in detail. Different laser fluences are used in the simulation to explore how and to what extent the energy input affects the dynamic melting behavior and the final dimension and profile of the surface nanostructure. In-depth theoretical investigation gives satisfactory explanation of the effect of the laser fluence on the melting depth. Spot-like structural defects in the sub-surface region are observed and investigated until full solidification.

© 2008 Elsevier B.V. All rights reserved.

Keywords: Effect of laser fluence; Surface nanostructuring; Molecular dynamics simulation

1. Introduction

In laser-assisted manufacturing and material processing, the diffraction effect limits the minimum size of the focused laser beam, making it difficult to reach nanoscale manufacturing feature sizes. In the past decade, various techniques have been developed to overcome the diffraction limit to achieve laser-assisted nanomanufacturing. Nanoscale focusing of laser light is made possible by using different near-field techniques, such as near-field scanning optical microscopy (NSOM) [1], superlens, nanoscale aperture, and scanning probe microscopes (SPM). In work by Fang et al. [2], a silver coating was used as a natural optical superlens to demonstrate a sub-diffraction-limited imaging with 60-nm half-pitch resolution, or one-sixth of the illumination wavelength. Jin and Xu [3] employed nanoscale aperture as a highly efficient near-field radiator. Nanoscale radiation spots with an efficiency larger than unity can be achieved in the near field. In work by Wang et al. [4],

C-shaped ridge apertures were used in contact nanolithography to achieve nanoscale resolutions. In Lu's work [5], the SPM was utilized as a significant technique to develop a novel nanofabrication method. The scanning tunneling microscopy (STM), as one important subdivision of SPM, is a promising tool in surface nanostructuring. In laser-assisted STM, upon laser irradiation, the tip acts as a receiving antenna to collect the laser energy and then acts as a transmitting antenna to create a significantly enhanced optical field in proximity to the tip apex. This optical field could be enhanced by 2 orders of magnitude [6]. The enhanced optical field could heat the sample surface and induce phase change and modify the surface at nanoscales [7–16]. Similar to STM, atomic force microscope (AFM) has been used to focus the laser beam to a nanoscale spot for surface nanostructuring [15–17].

In surface nanostructuring with an extremely focused near-field laser beam, as a direct consequence of nanoscale heating, a nanodomain of the sample will experience intense heating, phase change/explosion, stress development and propagation, and rapid structural evolution. Although a large number of work has been reported to study the enhanced optical field, light confinement, and nanoscale heating [18–24], very little

* Corresponding author. Tel.: +1 515 294 2085; fax: +1 515 294 3261.
E-mail address: xwang3@iastate.edu (X. Wang).

experimental work has been conducted to study the phase change and structural evolution in nanomanufacturing/structuring, probably due to the extremely small scale involved in the process. At nanoscales, thermal movements of molecules/atoms will be endowed with strong statistical uncertainties since thermal equilibrium cannot be well established. Continuum approaches will fail to predict the above physical processes. Molecular dynamics (MD) simulation, which directly tracks and analyses the movement of molecules/atoms, is capable of exploring the physical phenomena down to molecular/atomic levels. In recent work by Wang [25,26], the thermal, mechanical, and structural phenomena in surface nanostructuring with a picosecond laser-assisted STM was studied by using large-scale parallel MD simulation. One work by Wang [25] focused on the physical processes during laser heating and within a short time after laser heating (up to 500 ps). In surface nanostructuring, the final surface nanostructure is strongly affected by solidification of the molten material. The solidification process is driven by the heat conduction in the material and is much slower than the heating and melting processes that are directly driven by the laser energy input. Another work by Wang and Lu [26], using large-scale parallel MD simulation, explores the laser irradiation and following long-time (up to 2 ns) solidification behavior during the surface nanostructuring. However, full solidification was not studied and the nanostructuring happened in a relatively large domain (more than 100 nm). Very little knowledge has been obtained about how the laser pulse energy affects the dimension and profile of the final surface nanostructure.

Targeting the above knowledge gap, this research focuses on how and to what extent the laser fluence affects the final dimension and surface profile in nanostructuring. Three domains and eight laser fluences are used in this systematic modeling. Furthermore, extensive MD simulations are also performed to study the long-time behavior of materials in surface nanostructuring from the initial heating until full solidification. Section 2 gives a brief introduction to the methodologies used in this simulation. Section 3 presents detailed result about the laser heating and solidification process, defect evolution in solidification, and the effect of laser fluence and domain size on the resulting surface nanostructure.

2. Methodologies of simulation

The methodologies used in this simulation have been detailed in our previous work [25,26]. Therefore, only a brief introduction is given in this section about how the physical domain is designed and how the laser heating is arranged. Fig. 1 shows the schematic of a free-standing thin film (detailed size

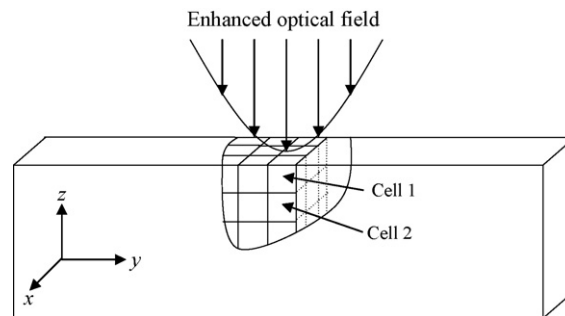


Fig. 1. Schematic of the simulation configuration and laser absorption (not to scale).

information is listed in Table 1) modeled in this work, which is under the irradiation of an enhanced optical field. Argon at 50 K is chosen as the film material due to its well-established potential and convenience of computation. Different from our previous work [25,26], the physical domain in the x direction in this work is reduced to 5 face-centered cubic (FCC) units, which are enough for capturing the physical phenomena, and can also substantially reduce the computational burden. This domain size is much smaller than those in the other two directions (Table 1), meaning this sample can be considered quasi 3-dimensional. Therefore, the physical characteristic distribution in the y - z plane is our primary research interest. This domain design makes it feasible to conduct MD simulation to a much-extended time and capture the long-time behavior of the material from heating to full solidification.

In this MD modeling, the Lennard–Jones (LJ) potential is used to simulate the movement of argon atoms. The LJ well-depth parameter (ϵ) and equilibrium separation (σ_e) is 1.653×10^{-21} J and 3.406 Å, respectively. The atomic mass of argon takes 66.3×10^{-27} kg, and the lattice constant is 5.414 Å. In this work, the half-step leap-frog scheme is used [27]. The cut-off distance r_c takes $2.5\sigma_e$ and is used to arrange the computational domain for efficient atom sorting and computation. The linked-list method [27] is also employed to arrange the atoms and their neighbors in each cell, which is helpful to locate every single atom and obtain its position and velocity in a quick manner. The computational time step is 25 fs ($1 \text{ fs} = 10^{-15} \text{ s}$).

The focused near-field laser beam is assumed to have a temporal and spatial distribution as

$$I = I_0 \exp\left(\frac{-(\vec{r} - \vec{r}_0)^2}{r_g^2}\right) \exp\left(\frac{-(t - t_0)^2}{t_g^2}\right) \quad (1)$$

where I_0 is a laser beam intensity constant, \vec{r}_0 the center of the sample surface, r_g ($=5 \text{ nm}$) the length constant determining the

Table 1
Detailed information about the three domains studied in this work

	Sample 1	Sample 2	Sample 3
FCC cubes in the domain ($x \times y \times z$)	$5 \times 324 \times 60$	$5 \times 648 \times 60$	$5 \times 324 \times 120$
Domain size (nm^3)	$2.707 \times 175.4 \times 32.48$	$2.707 \times 350.8 \times 32.48$	$2.707 \times 175.4 \times 64.97$
Atom number	388,800	777,600	777,600

size of the laser beam, t_0 (=10 ps) the peak time, and t_g (=3 ps) a time constant affecting the pulse width. The laser pulse distribution in Eq. (1) is constructed for convenience of computing. The full-width at half-maximum (FWHM) of the laser pulse is 5 ps centered at 10 ps.

Fig. 1 also shows the numerical treatment of the laser absorption in the sample. The physical domain is divided into computational cuboid cells, whose size is a little larger than the cut-off distance. The propagation of laser in the material is along the z direction layer by layer. As shown in Fig. 1, Cell 1 is the first cell to absorb the laser energy. The laser energy reaching Cell 1 within a time step (δt) is $E_1 = \int_A I \delta t dA$, where A is the top surface area of Cell 1. During each time step, the density of atoms within cell 1 will be calculated as ρ_1 . In this simulation, an artificial absorption depth ($\tau = 10$ nm) is chosen to reflect the volumetric absorption of the laser beam in the sample rather than to represent the practical experimental condition. Due to heating, explosion and other physical processes, the real optical absorption depth of Cell 1 is adjusted to be $\tau_1 = \tau \rho_0 / \rho_1$, where ρ_0 is the density of argon at 50 K. Therefore, the laser energy absorbed by Cell 1 within each time step is

$$\delta E_1 = E_1 \left(1 - \exp\left(\frac{-\delta z}{\tau_1}\right) \right) \quad (2)$$

where δz is the size of Cell 1 in the z direction, and an artificial absorption depth (τ) of 10 nm is employed as mentioned before. After the absorption in Cell 1, the remaining laser energy arriving at Cell 2 is $E_2 = E_1 - \delta E_1$. In Cell 2, the same absorption procedure is considered and the absorbed laser energy can be calculated using the above formula. This process repeats in all cells until the energy is totally absorbed by the material, so that the laser energy can propagate into the interior of the sample. The laser beam absorption in the material is achieved by exciting the kinetic energy of atoms while the momentum of atoms is conserved during laser beam absorption. More details of the computational principles and laser energy absorption can be found in our recent work [25,26].

3. Results and discussion

Three samples of different domain sizes are simulated. Table 1 summarizes the detailed information about the samples, including their domain sizes and number of atoms. These samples are constructed to have the x direction length much shorter than the beam spot (~ 5 nm). The pulse energies applied in this work are chosen as 0.05, 0.1, 0.2, 0.35, 0.5, 0.75, 1 and 1.1 fJ (1 fJ = 10^{-15} J). The corresponding maximal energy density levels are about 12, 24, 48, 84, 120, 180, 240, and 260 MW/cm², respectively.

Before applying laser heating, a velocity scaling simulation is performed for 4000 steps (100 ps) to make the sample reach the desired initial temperature of 50 K. Then an equilibrium calculation is performed for 4000 steps to eliminate the disturbance introduced by the velocity scaling. During simulation, periodical boundary conditions are applied in the x and y directions, and free boundary conditions in the z direction. Free

spaces are added below and above the sample to allow extended atom movement in the z direction. Finishing the full solidification until 5 ns requires a simulation up to 30 days using a single computer. Parallel computation scheme is employed in this work to realize the periodic boundary condition in the y direction. For large-scale computation, the physical domain can be divided into many sub-domains of the same size. These sub-domains are distributed over nodes of a computer cluster. Each node is responsible for the MD simulation of one sub-domain. The parallel program is developed using MPICH. Details of the parallel treatment are discussed in our recent work [25].

3.1. Overview of laser-induced nanoscale phase change

Before discussing the effect of the computational domain and laser fluence on the final surface nanostructure, this section is intended to provide a general picture about the entire nanostructuring process until full solidification. Fig. 2 shows the snapshots of atomic positions for sample 3 in the y - z plane. In this case, the laser energy takes 0.5 fJ. In these plots, each dot represents an atom. The plots from 1 to 100 ps mainly demonstrate the laser-induced heating, melting and vaporization procedure. Detailed discussion about this procedure can be found in our previous work [25,26]. From 100 to 500 ps, the surface tension force makes the liquid region become smooth gradually, and a distinct hole emerges right at the spot heated by the laser beam. Very few droplets are observed at 0.5 ns.

In this paper, our interest is the solidification process after laser heating. This process is clearly shown in the plots from 500 ps (0.5 ns) to 5 ns. Comparing the plots at 0.5 and 1 ns reveals that the two sides of the liquid region in the nanohole solidifies first and its solidification speed is faster than that at the bottom [26]. This is because the heat conduction area at the two sides of the nanohole is much stronger than that at the bottom. In the following figures from 2 to 5 ns, a long-time solidification procedure is observed, but the cone-shaped hole along with two adjacent protrusion regions becomes stable without appreciable evolution. The edge of the protrusion parts becomes smooth. Meanwhile, the region adjacent to the heated surface evolves back to a regular and ordered structure, leaving no obvious dark area (melt) in the sub-surface region.

To illustrate the laser-induced temperature distribution in sample 3, and to better explore the solidification and crystallization in the whole process, we plot out the y - z plane temperature distribution in Fig. 3. Because in MD simulation the temperature is derived from the average molecular kinetic energy, the temperature can be viewed as a representation of the molecules' intense movement. It is observed that after the equilibrium procedure, the whole sample stays at 50 K ($t = 1$ ps). At 10 ps, the focused laser beam has heated the central spot of the sample surface for a while, so the local temperature increases to a level as high as 320 K. Due to heat conduction, the temperature of the neighboring area close to the heated region also goes up to 80–140 K. Since the melting point of argon is 83.8 K, it is obvious that the heated argon in the nanohole makes this region become liquid. At 20 ps, the highest temperature is not as high as that at 10 ps, and the heated region

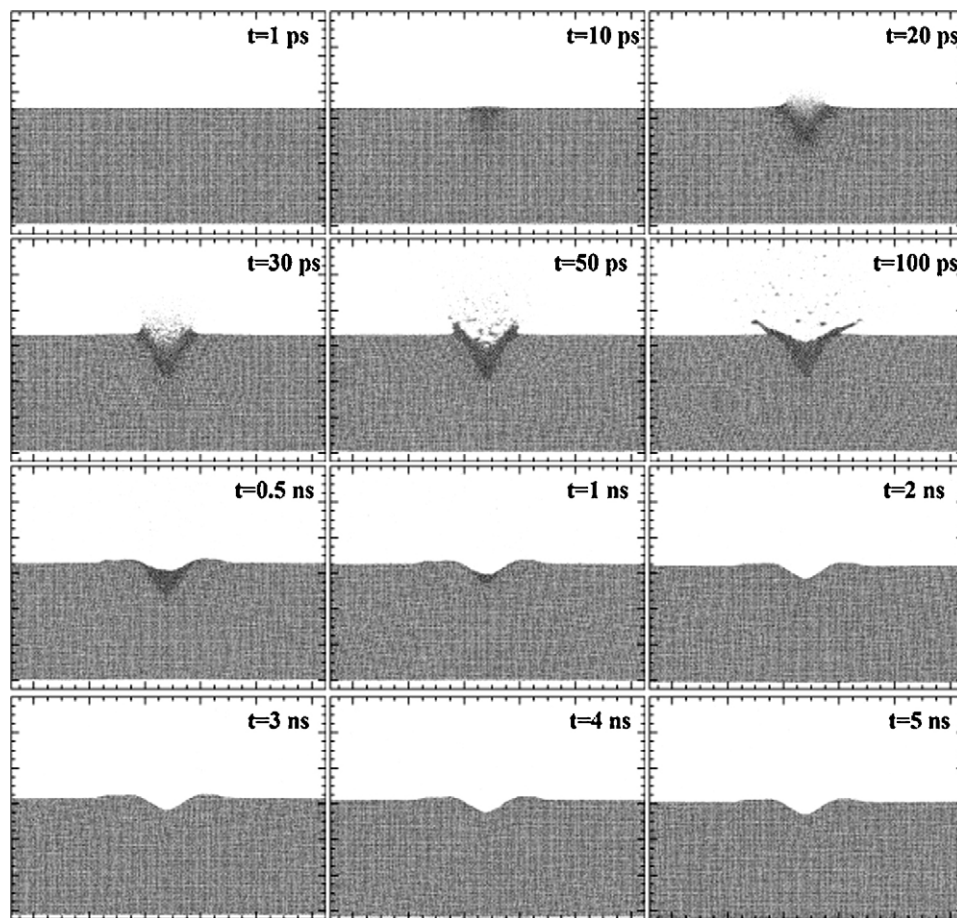


Fig. 2. Snapshots of atomic positions in the y (horizontal: 32–145 nm)– z (vertical: 175–300 nm) plane 2.707 nm-thick. Only part of the sample is displayed in order to show details of the nanostructuring region. The sample in this figure is sample 3, and the laser fluence is 0.5 fJ.

becomes larger because of heat conduction. After 30 ps, the laser heating stops (at 30 ps), and the laser-induced heat is conducted away. The temperature of this region goes down to around 80 K and an evident explosive phenomenon happens, just as shown in Fig. 2. When the argon atoms obtain enough energy, which can break the interaction bonds and destroy the original crystal structure, the atoms can move away from early positions without restriction. Some of them fly out of the surface with tremendously high velocity, causing an obvious vacant area in the sample surface. At 500 ps, the hole induced by laser heating remains, and the edge becomes smooth. The temperature of the heated region drops into a range of 60–80 K. As mentioned before, the melting point of argon is 83.8 K, thus the nanohole starts to solidify. After 4 ns, it can be found that during solidification, the thermal energy left by heating gradually dissipates by conduction, and the whole sample temperature decreases to around 50 K, only leaving a few hot spots (~ 60 K). This temperature distribution indicates that the solidification and crystallization process finishes completely.

3.2. Effect of the computational domain on simulation results

In surface nanostructuring with an extremely focused laser beam, the strong and localized heating can generate strong

stress in the material. Since the bottom of the sample takes free boundary conditions in our modeling, when the stress wave reaches the bottom, it will be reflected back to the nanostructuring region. This phenomenon and corresponding theoretical analysis have been discussed in our recent work [25]. It is possible that this reflected stress can affect the solidification procedure and the final surface nanostructure [28]. In this work, the computational domain is chosen to be large enough. Therefore, after the stress wave is reflected to the surface region, their amplitude could become weak to induce negligible effect on the final surface nanostructure. Different domain sizes (listed in Table 1) are used in this work to explore how the domain size affects the final surface structure.

The final surface profiles of the three samples are presented in Fig. 4, in which the chosen laser pulse energy is 0.5 fJ, and all the data are obtained at 4 ns up to which full solidification is reached. The profiles are shifted a little bit along the y -axis for ease of comparison. This figure shows that the difference of computational domains does not induce evident influence on the final surface nanostructure. All the three nanostructures finally have almost the same shape. The bottom of the nanohole in sample 2 is a little lower than that of the other two. When materials are ejected from the nanohole during laser heating, due to momentum conservation, the recoil pressure will push the sample to move in the $-z$ direction. Because sample 2 is

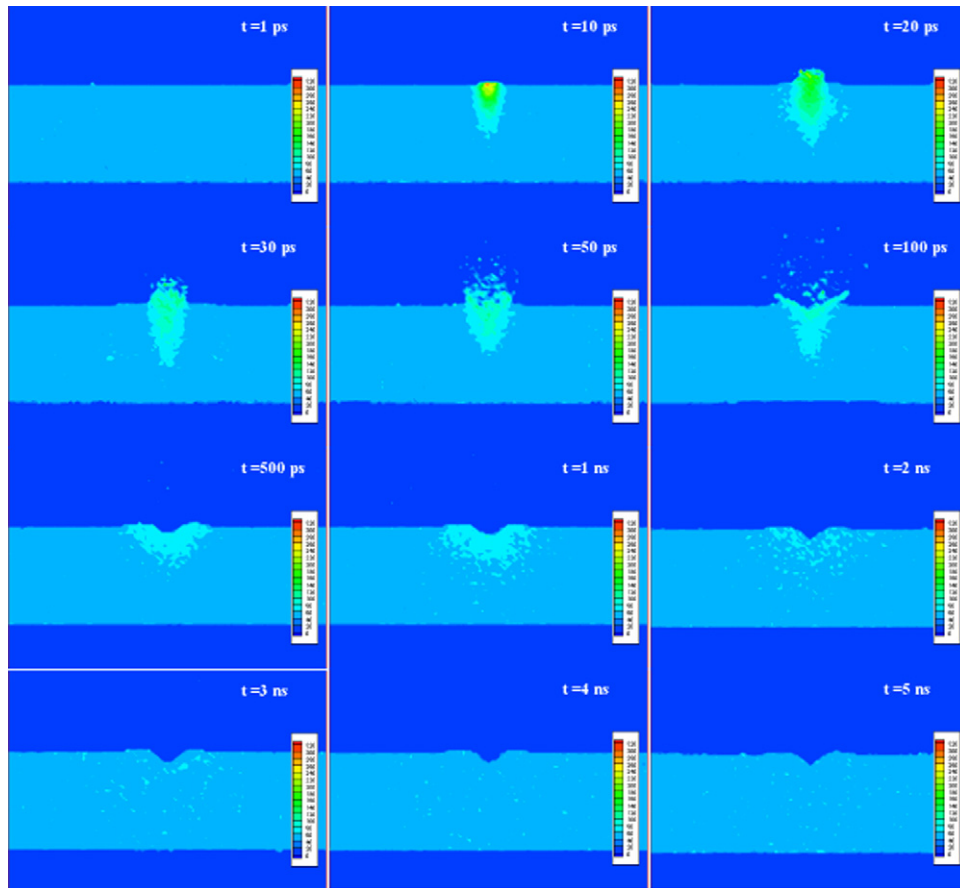


Fig. 3. Temperature distribution in the y (horizontal: 0–175 nm)– z (vertical: 150–300 nm) plane 2.707 nm-thick. The domain in this figure is sample 3, and the laser pulse energy is 0.5 fJ.

longer in the y direction, making it more flexible in the z direction, therefore a more appreciable movement of the nanohole in the $-z$ direction is induced.

In order to analyze surface nanostructure quantitatively, characteristic geometric parameters are defined to describe the nanohole profile. Definitions of the profile parameters are shown in the inset in Fig. 4. ϕ is the distance between the two

peaks of the edge protrusion, h_1 is the distance from the average surface position to the bottom of the nanohole, and h_2 is the thickness of the nanohole edge. Detailed data of the plots in Fig. 4 are presented in Table 2. Considering the simulation uncertainty, these tiny differences can be accepted in the surface nanostructure using the three different computational domains under irradiation of the same optical field.

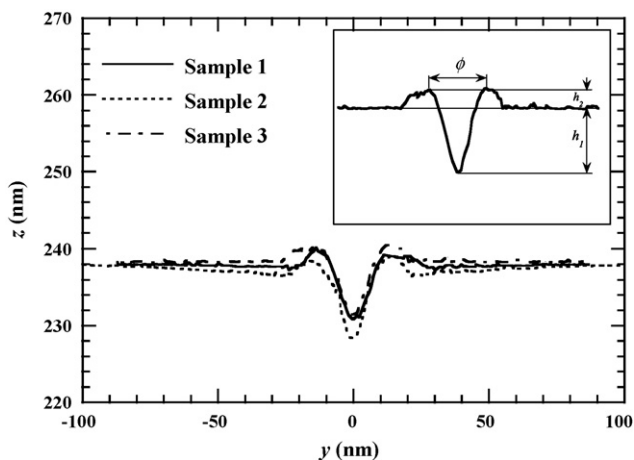


Fig. 4. Surface nanostructure profile comparison with the same laser fluence (0.5 fJ) and at the same time (4 ns). The inset shows the definition of the surface profile parameters.

3.3. Effect of the laser fluence on final surface nanostructure

In this work, eight different laser fluences are used to study the effect of the laser fluence on the final nanostructure: 0.05, 0.1, 0.2, 0.35, 0.5, 0.75, 1.0 and 1.1 fJ per pulse. No surface reflection is considered and these energies are totally absorbed by the sample. In all the simulation cases, sample 3 is the only one which has been irradiated by all laser fluences, and our discussion will focus on surface nanostructuring with sample 3. The surface nanohole profiles of sample 3 under different laser fluences are shown in Fig. 5. It is observed that when the laser fluence is as high as 1.0 and 1.1 fJ, the surface nanoholes caused by laser heating are the most evident, and the diameter and depth of the holes are the largest. In addition, the hillock on the edge of the hole is not regular and smooth, meaning intense and disturbed liquid movement during the formation of nanoholes. As the laser fluence is reduced to 0.5 and 0.35 fJ, the hole in the

Table 2
Characteristic sizes describing the final nanohole profile with 0.5 fJ laser energy for three different domain sizes

	Sample 1: $5 \times 324 \times 60$	Sample 2: $5 \times 648 \times 60$	Sample 3: $5 \times 324 \times 120$
ϕ (nm)	24.83	27.90	27.76
h_1 (nm)	6.400	8.809	7.693
h_2 (nm)	2.432	2.370	2.678

surface gets smaller, and the edge of the hole is more regular and smoother. When the laser energy is 0.2, the dent is much shallower, meanwhile the edge is only a little higher than the surface. When the laser fluence is as low as 0.1 and 0.05 fJ, the holes in the surface are almost invisible, but the surface under 0.05 fJ is flatter than the surface under 0.1 fJ, in which a tiny irregular change in the middle can be seen. Our detailed study of the surface under 0.1 fJ shows that a few atoms are removed from the heating area.

In Fig. 5 it is also observed that when the solidification procedure finishes, the nanostructure at 1.1 fJ has the lowest z location. As mentioned before, when atoms explode from the surface, because of momentum conservation, the rest part of the sample will move along the opposite direction. When the laser energy is higher, more atoms will escape from the surface, thus the momentum of the sample derived by the ejected atoms is larger, making the entire film move further along the opposite z direction. When the laser energy is as high as 1.1 fJ, the final sample surface is as low as 233 nm, moving more than 10 nm from its original position of 245.23 nm. As the laser energy decreases, the final surface position does not move that far from its original position. For instance, when the laser pulse energy is 0.5 fJ, the surface has moved only 3 nm. The three curves with lower energies (0.05, 0.1, and 0.2 fJ) show that their final surface positions almost have no change during the whole procedure, meaning the atoms escaping from these samples are much fewer.

Another comprehensive and detailed comparison for the impact of the laser fluence on the final surface nanostructure is shown in Fig. 6. Calculations have been conducted for samples 1 and 2, and no appreciable difference about the surface

nanostructure is observed compared with that for sample 3. Therefore, Fig. 6 only shows the calculation result for sample 3. In Fig. 6, the values of h_1 under different laser fluences clearly show that when the laser fluence increases from 0.2 to 1.1 fJ, the depth of the final nanostructure also increases. As to the characteristic sizes h_2 and ϕ , when laser fluences are lower than 0.75 fJ, the value of both characteristic sizes shows accordant increase with the laser fluence. But when the laser fluence reaches around 0.75 fJ, the values of h_2 and ϕ show a slight unconformity with laser energy, meaning that 0.75 fJ might be an energy threshold below which the sample can present a distinct and gentle final nanostructure without intense surface explosion and irregular nanostructure. In order to not to destroy the material, this energy threshold is important for surface nanostructuring. It also can be learnt from Fig. 5 that when the laser fluence is lower than 0.75 fJ, the two edge apexes are very distinct and regular. However, in the plots in which the laser fluences are higher than 0.75 fJ, the edge apexes are not so regular and distinct, which means the laser fluence might be a little strong and the surface has endured an intense heating and explosion, thus the final nanostructure has been slightly altered. In this case, the values of h_2 and ϕ may be a little unconformity and have some unexpected changes with the increasing laser fluence. What can be anticipated is that when the laser fluence goes higher than 1.1 fJ, the final surface nanostructure would feature more irregularity.

3.4. Structural evolution under different laser fluences

In our previous work [25,26], structural defects have been observed in laser heating and the solidification procedure. The

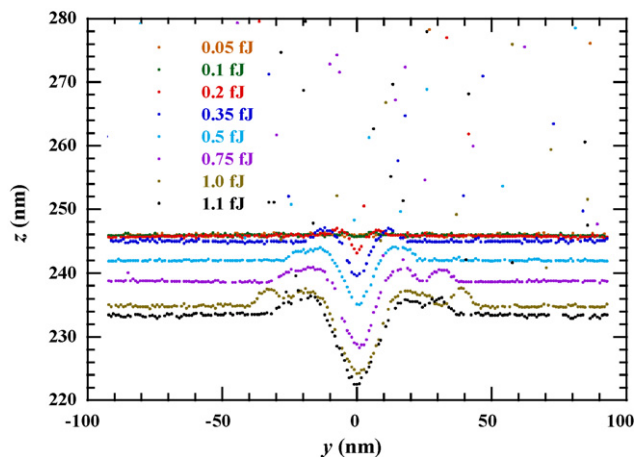


Fig. 5. Final surface profile comparison for sample 3 under different laser fluences after complete solidification.

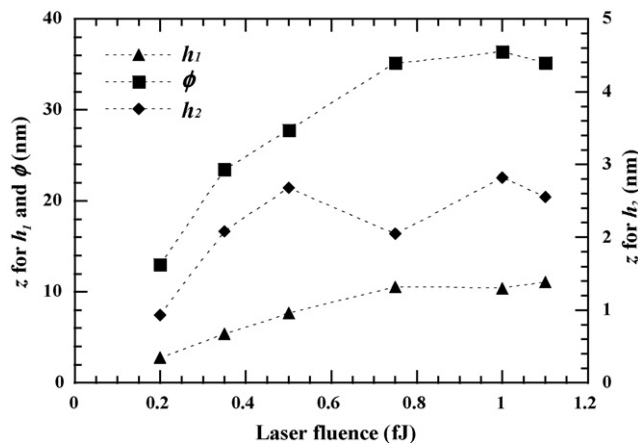


Fig. 6. Effect of the laser fluence on the final surface nanostructure after complete solidification.

focused laser beam has a relatively large beam spot (~ 50 nm), and the structural defects are observed as nanoscale lines with atomic dislocations inside. In this work, the structural defect is studied up to full solidification. To illustrate the structural defects, a crystallinity function designed in our previous work [26] $\Phi(r_{i,z})$ is used

$$\Phi(r_{i,z}) = \frac{1}{N} \left| \sum_i e^{j2\pi \cdot 2r_{i,z}/\lambda} \right| \quad (3)$$

where $r_{i,z}$ is the z coordinates of atom i , N is the number of atoms within the domain of interest, and λ is the light wavelength for structure study. In this work, λ takes the value of the lattice constant, a . This function works well to clearly identify the crystallization of the sample and to distinguish the liquid and solid regions. If atoms are regularly distributed in space with their spacing in the z direction equal to $n \cdot a/2$ (n : integer), the function $\Phi(r_{i,z})$ will be equal to 1, In liquid, the function $\Phi(r_{i,z})$ will be much less than 1. Detailed introduction to $\Phi(r_{i,z})$ can be found in work by Wang and Lu [26].

Fig. 7 shows the value distribution of the crystallinity function defined by Eq. (3) after laser heating until full solidification for sample 3 under 0.5 fJ laser heating. As shown in Fig. 7, at 0.5 ns, the heated cone-shaped region is filled with liquid. When the solidification process continues to 1 ns, the liquid region is obviously becoming smaller, showing very appreciable solidification. From the comparison of the first two plots, it can be seen that the crystallization speed of the two sides of the hole is much faster than that of the bottom, for the conduction area of both sides is much larger. Careful observation reveals that after 1 ns, in the region close to the bottom of the nanohole, a small green spot, where $\Phi(r_{i,z})$ is about 0.5, emerges and remains in the solidification procedure. As mentioned above, the function value shows the crystallinity of the material. The value 0.5 suggests that the structure regularity of this point is not so good compared to other solid regions of the sample. In Fig. 7, Details of this structural defect are shown in the inset of the plot at 2 ns. In the solid region, the atomic alignment is very regular, while the defect region shows random atomic alignment. In our former study, some atomic

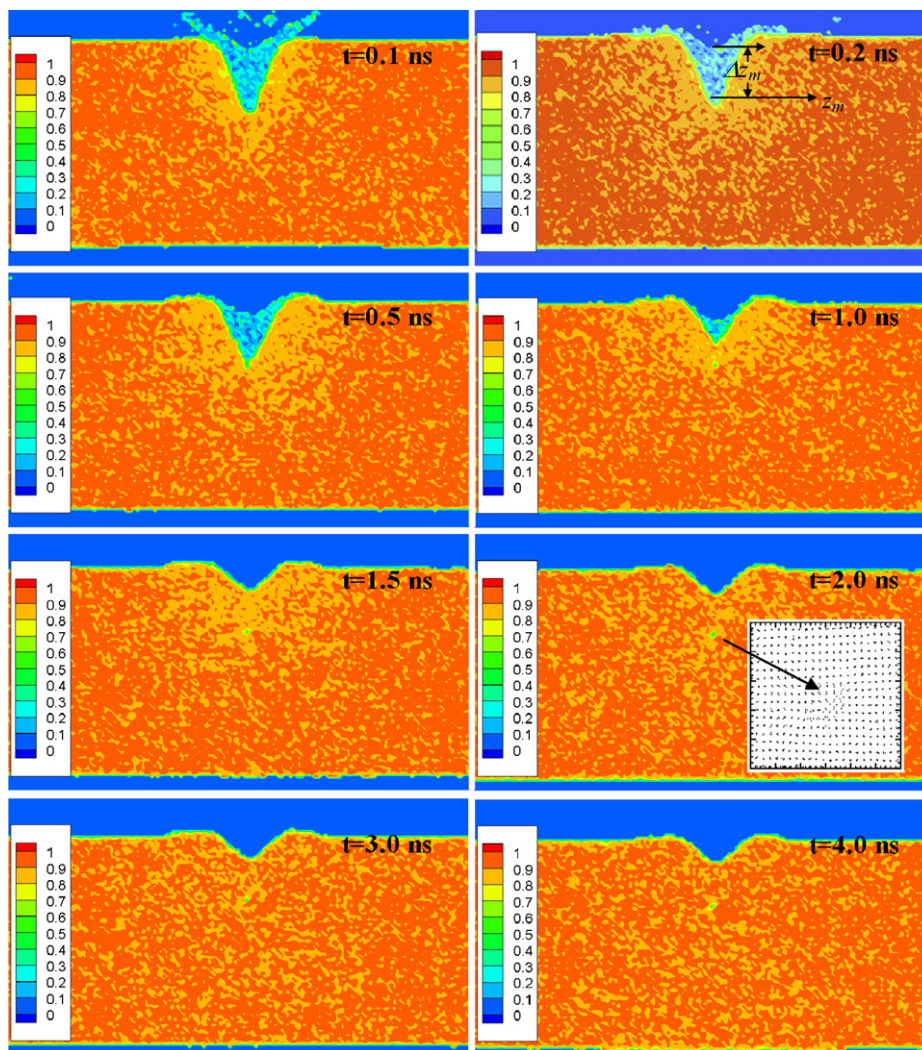


Fig. 7. The distribution of $\Phi(r_{i,z})$ at different times in the y (horizontal: 17–162 nm)– z (vertical: 175–285 nm) plane for sample 3 irradiated with 0.5 fJ laser pulse. Additionally, in the plot of 0.2 ns, two denotations are defined: Δz_m is the largest melting thickness, and z_m is the lowest melting position. The inset in the plot of 2 ns is a magnified image of the atomic defect forming during the crystallization.

defects which are introduced by the stress wave propagation were observed [25]. However, instead of a line [25], the defect in this simulation is featured with a spot-like shape. This spot-like shape is possibly attributed to the extremely localized thermal stress in the region heated by the enhanced near-field laser beam. It is expected this spot-like defect and its irregular atomic distribution can significantly enhance the local phonon scattering and reduce the local thermal conductivity.

With function $\Phi(r_{i,z})$, the above discussed melting and solidification procedure under different laser fluences can be revealed quantitatively from another aspect. Using this function, the melting thickness and the lowest melting point in the material are studied. In Fig. 7, as shown in the plot of 0.2 ns, these two parameters are defined as: Δz_m is the thickness of the molten material in the laser incident direction, and z_m is the lowest melting position. Fig. 8 shows the evolution of these parameters during laser heating and solidification. The lower curves in Fig. 8(a) show the evolution of the melting thickness under different laser fluences. This melting thickness reflects the characteristic heat-affected zone in the laser incident direction. Also shown in Fig. 8(a) is the normalized laser pulse shape. When the laser fluence is 0.2 fJ, the evolution curve is smooth and quite flat, and its largest melting thickness is only around 10 nm. As the energy goes up, such as 0.35 and 0.5 fJ,

their curves have more oscillation with time than that of 0.2 fJ, demonstrating an intense heating and melting process. It is observed that with the laser fluence increasing, the starting time for melting becomes earlier, which is due to the higher temperature rise induced by larger laser fluences. Fig. 8(a) also shows that after the laser pulse stops, the melting does not stop immediately, but still goes on for a certain time. At 0.2 fJ laser fluence, it takes the shortest time (0.02 ns) for the surface melting to reach the largest melting thickness. For 1.0 fJ laser fluence, the melting will continue to almost 0.1 ns. Quantitative display of the time taken to reach the largest melting thickness is shown in Fig. 8(b). Also shown in Fig. 8(b) is how the largest melting thickness changes with the laser fluence. The largest melting thickness shows almost linear increase with the laser fluences. But when time is referred to, it shows an oscillating change with the laser fluence. The trend of this curve still presents that the higher laser fluence, the longer time it takes to reach the largest melting thickness.

3.5. Theoretical analysis of the effect of the laser fluence on melting depth

In this section, in-depth theoretical analysis is performed to explain the effect of the laser fluence on melting depth observed in MD simulation. In our simulation, the modeled material (Ar) has a very low thermal conductivity (~ 0.5 W/m K) [29]. In addition, the laser heating time is very short, in the order of 10^{-11} s. Therefore, it is physically reasonable to assume that the heat conduction has negligible effect on phase change during laser-material interaction. Under this assumption, the temperature increase (ΔT) of the material is in the form of (without considering melting yet):

$$\Delta T = \Delta T_0 \exp\left(\frac{-(r-r_0)^2}{r_g^2}\right) \exp\left(\frac{-z}{\tau}\right) \quad (4)$$

where ΔT_0 is a constant whose exact value can be calculated based on laser energy absorption, and τ is the absorption depth. Combining Eqs. (1) and (4), and applying energy balance for the domain, the following equation can be derived,

$$\rho c_p \Delta T_0 \int \exp\left(\frac{-z}{\tau}\right) dz = I_0 \int \exp\left(\frac{-(t-t_0)^2}{t_g^2}\right) dt \quad (5)$$

If certain integral limits are applied to both sides of Eq. (5), relationships between the time and melting thickness can be obtained, and ΔT_0 can also be obtained. To give the first order estimation of the melting depth, the values of density (1673 kg/m³) [30] and heat capacity (709.9 J/kg K) [30] of argon at 65 K are used since 65 K is around the middle point between the initial temperature (50 K) and the melting point of argon (83.8 K). Although the melting point of Argon is 83.8 K, the material phase transition would not take place even when the temperature reaches this point since extra energy is needed as the latent heat. The latent heat, which is an additional energy for overcoming the inter-atomic bonds and causing the phase to transit from solid to liquid, needs to be considered in theoretical analysis. For argon at 83.8 K, the latent heat is 27.44 kJ/kg [31].

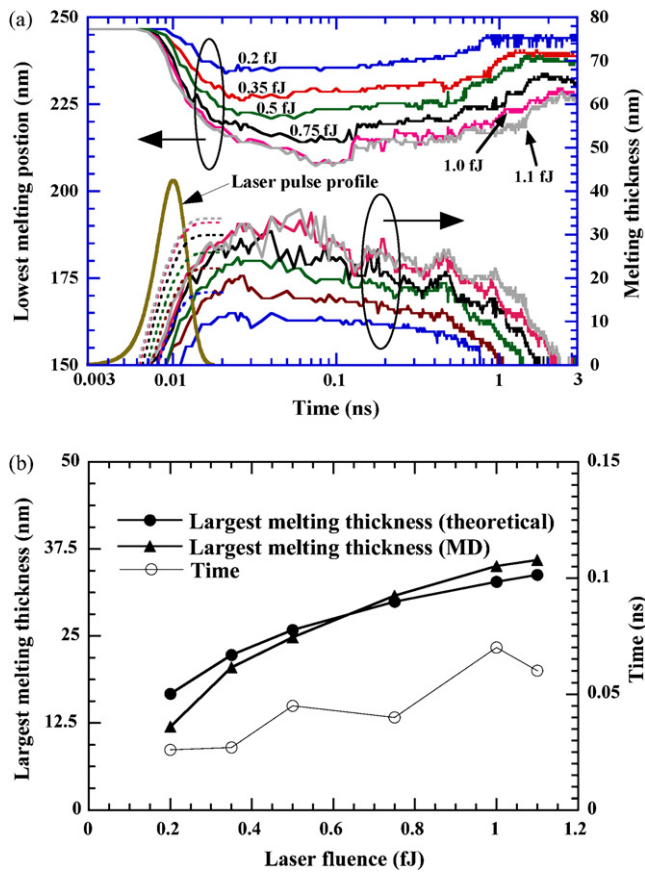


Fig. 8. (a) Thickness evolution of the molten material and lowest melting position in sample 3. The same color of the curves is for the same laser fluence as indicated in the figure. The dashlines are for the theoretical analysis. (b) Variation of the largest melting thickness vs. the laser fluence. Also shown in the figure is the time taken to reach the largest melting thickness.

For complete melting, the temperature of solid argon needs to be elevated 31.47 K above its melting point at the solid state. This excessive temperature rise (31.47 K) above the melting point is needed to compensate for the latent heat, and is calculated using the heat capacity 872 J/kg K [30] at 83.8 K. Therefore, in the solid target material's transiting from solid to liquid, the required total temperature rise is 65.27 K when the initial target temperature is 50 K.

From Eq. (5), it is seen that part of the solid material will have a temperature rise between 33.8 and 65.27 K. For this part of the solid material, the excessive energy above the melting point will also be used to melt some solid. Eq. (5) shows that the solid will have a temperature distribution following the form of $\exp(-z/\tau)$ between 33.8 K (z_1) and 65.27 K (z_2). It is readily to calculate that a material 4.82 nm thick will also be melted between z_1 and z_2 by the excessive energy above 33.8 K. This melting thickness should be added on top of the thickness determined by the temperature rise 65.27 K described above to give the whole melting thickness in the target.

In Fig. 8(a), the analytical results are represented by dashed line, and in Fig. 8(b) the analytical largest melting thickness under different fluences is also presented. In Fig. 8(b), the analytical results are in good agreement with the MD simulation results with a small difference because of the assumptions in the theoretical deduction. In the theoretical calculation, we have not considered heat conduction. But in practical MD simulation, this kind of heat conduction takes place and reduces the temperature increase of the material in the near surface region. For low laser energy input, this heat conduction is relatively important in comparison with the whole energy input, therefore the above theoretical analysis gives an over-evaluated melting thickness compared with the MD simulation result at low laser fluences. For higher energy input, the heat conduction effect becomes much less important in comparison with the total energy input. Further investigation has been done to support this conclusion. For two different energy fluences, such as 1.1–0.2 fJ, their energy input ratio is 5.5. But during their melting procedures, the ratio of effective heat conduction area (defined by the solid–liquid interface) for energies 1.1 and 0.2 fJ is only 2.3, meaning the heat conduction effect is becoming less important when the energy input is higher.

When the laser energy goes higher, Fig. 8(b) shows that the MD results are even higher than the theoretical analysis. This is because in our theoretical study, a distinct vertical temperature gradient is assumed, which can be seen in Eq. (4). This means some excessive energy in the surface region is not used to melt the material. On the other hand, in MD simulation it is found that in the melt the temperature gradient is not so sharp, just a little above the melting point. Therefore, the same energy input will induce a larger melting thickness in the MD simulation. In Fig. 8(a), the dashed lines describe the theoretical calculation results for the dynamic behavior of melting. These theoretical results show similar tendency with the MD simulation in the heating procedure. But in MD simulation, even when the temperature reaches the melting point, melting cannot happen immediately and takes some time to occur since the material needs to obtain enough energy to melt. Such phenomenon is not

considered in the theoretical analysis. This explains the earlier melting by the analytical results in comparison with MD simulation. Another reason for the earlier melting in the analytical results is that no heat conduction is considered; therefore the surface region will experience higher temperature increase and earlier melting. After the laser stops, since the melting region is above the melting point, heat conduction from the melt to solid will continue melting the material for a little while. This explains why the melting stops later in MD simulation than the theoretical analysis shown in Fig. 8(a).

During the melting and solidification procedure, the solid surface melts and sinks, and the interface between the liquid and solid regions emerges. The position of this interface provides a characteristic measure of the nanostructuring process and the laser-affected zone. This position is influenced by both melting and solidification processes, as well as bending of the sample by the recoil pressure. In Fig. 8(a), the upper curves show the evolution of the lowest position of the solid–liquid interface. At the very beginning, the laser energy is not strong enough and the surface does not change. As time goes on, the central part of the sample surface begins to melt and the interface emerges. The higher the laser fluence, the earlier the interface emerges, like the evolution of melting thickness discussed above. After the heating stops, because the absorbed heat still needs time to be conducted away, the melting still goes on further and the interface keeps moving down until an equilibrium point is reached. Then the molten part starts to solidify and the interface begins to retreat. For different laser fluences, the time taken for the melting to stop is also different, showing very similar trend like that for the melting thickness.

4. Conclusion

In this work, MD simulations were conducted to study the long-time (up to 5 ns) behavior of argon crystal in surface-nanostructuring with near-field focused laser beam. The research focused on the effect of computational domain and laser fluence on final surface nanostructuring. MD simulations were performed for three samples of different domain sizes, and with eight different levels of laser beam energy input. Our study of the impact of domain size showed that if the computational domain was chosen reasonably large, the reflected stress from the bottom of the sample will have negligible effect on the final nanostructure. The laser fluence showed strong effect on the diameter, depth, and edge protrusion of the surface nanostructure. The increase of these parameters with the laser fluence slowed down and showed slight oscillation when the laser fluence is above a threshold. Thermal strain-induced structural defect was observed in the solidification procedure. Because of the extremely localized laser heating, the defect was featured with a spot-like shape, different from the line-shape structural defects observed in surface nanostructuring with a relatively large laser heating spot. Careful study of the solid–liquid interface and the melting thickness showed that after the laser heating stopped, because of heat conduction, melting procedure continued for a while to reach the largest melting thickness. An in-depth analytical investigation was performed about the

largest melting thickness and dynamic melting behavior. The results showed sound agreement with the MD simulation, explaining the physics behind the effect of the laser fluence on material melting.

Acknowledgements

Support for this work from NSF (CMS: 0457471), Nebraska Research Initiative, and Air Force Office for Scientific Research is gratefully acknowledged.

References

- [1] S. Toshiharu, N. Yoshihito, *JSAP Int.* 5 (2002) 22.
- [2] N. Fang, H. Lee, C. Sun, X. Zhang, *Science* 308 (2005) 534.
- [3] E.X. Jin, X.F. Xu, *J. Quant. Spectrosc. Radiat. Transfer* 93 (2005) 163.
- [4] L. Wang, E.X. Jin, S.M. Uppuluri, X.F. Xu, *Opt. Express* 14 (2006) 9902.
- [5] Y.F. Lu, B. Hu, Z.H. Mai, W.J. Wang, W.K. Chim, T.C. Chong, *Jpn. J. Appl. Phys.* 40 (2001) 4395.
- [6] Y.F. Lu, Z.H. Mai, W.K. Chim, *Jpn. J. Appl. Phys.* 38 (1999) 5910.
- [7] J. Jersch, F. Demming, K. Dickmann, *Appl. Phys. A* 64 (1997) 29.
- [8] Y.F. Lu, Z.H. Mai, Y.W. Zheng, W.D. Song, *Appl. Phys. Lett.* 76 (2000) 1200.
- [9] J. Jersch, K. Dickmann, *Appl. Phys. Lett.* 68 (1996) 868.
- [10] J. Jersch, F. Demming, L.J. Hildenhagen, K. Dickmann, *Appl. Phys. A* 66 (1998) 29.
- [11] Y.F. Lu, Z.H. Mai, G. Qiu, W.K. Chim, *Appl. Phys. Lett.* 75 (1999) 2359.
- [12] B. Hu, Y.F. Lu, Z.H. Mai, W.D. Song, W.K. Chim, *First International Symposium on Laser Precision Microfabrication*, 232, Omiya, Saitama, Japan, 2000.
- [13] Z.H. Mai, Y.F. Lu, S.M. Huang, W.K. Chim, J.S. Pan, *J. Vac. Sci. Technol. B* 18 (2000) 1853.
- [14] Z.H. Mai, Y.F. Lu, W.D. Song, W.K. Chim, *Appl. Surf. Sci.* 154–155 (2000) 360.
- [15] A. Chimmalgi, T. Choi, C. P. Grigoropoulos, *ASME International Mechanical Engineering Congress and Exposition*, New Orleans, LA, paper #33858, 2002.
- [16] S.M. Huang, M.H. Hong, Y.F. Lu, B.S. Lukyanchuk, W.D. Song, T.C. Chong, *J. Appl. Phys.* 91 (2002) 3268.
- [17] S. Grafström, *J. Appl. Phys.* 91 (2002) 1717.
- [18] W. Denk, D.W. Pohl, *J. Vac. Sci. Technol. B* 9 (1991) 510.
- [19] O.J.F. Martin, C. Girard, A. Dereux, *Phys. Rev. Lett.* 74 (1995) 526.
- [20] A. Madrazo, M. Nieto-Vesperinas, N. García, *Phys. Rev. B* 53 (1996) 3654.
- [21] O.J.F. Martin, C. Girard, *Appl. Phys. Lett.* 70 (1997) 705.
- [22] F. Demming, J. Jersch, K. Dickmann, P.I. Geshev, *Appl. Phys. B* 66 (1998) 593.
- [23] P.I. Geshev, F. Demming, J. Jersch, K. Dickmann, *Appl. Phys. B* 70 (2000) 91.
- [24] P.I. Geshev, F. Demming, J. Jersch, K. Dickmann, *Thin Solid Films* 368 (2000) 156.
- [25] X. Wang, *J. Phys. D: Appl. Phys.* 38 (2005) 1805.
- [26] X. Wang, Y. Lu, *J. Appl. Phys.* 98 (2005) 114304.
- [27] M.P. Allen, D.J. Tildesley, *Computer Simulation of Liquids*, Clarendon Press, Oxford, 1987.
- [28] M. Moseler, J. Nordiek, H. Haberland, *Phys. Rev. B* 56 (1997) 15439.
- [29] Y.S. Touloukian, *Thermophysical Properties of Matter*, vol. 3, New York, IFI/Plenum, 1970–79.
- [30] Y.S. Touloukian, *Thermophysical Properties of Matter*, vol. 6, New York, IFI/Plenum, 1970–79.
- [31] P.W. Bridgman, *Phys. Rev.* 46 (1934) 930.